J|A|C|S
JOURNAL OF THE AMERICAN CHEMICAL SOCIETY

Article

pubs.acs.org/JACS

Near-Infrared Absorbing $Cu_{12}Sb_4S_{13}$ and Cu_3SbS_4 Nanocrystals: Synthesis, Characterization, and Photoelectrochemistry

Joel van Embden,*[†,‡,#] Kay Latham,[§] Noel W. Duffy,[∥] and Yasuhiro Tachibana*[†,⊥]

[†]School of Aerospace, Mechanical & Manufacturing Engineering, RMIT University, Bundoora 3083, Victoria, Australia
[‡]Materials Science and Engineering, CSIRO, Bayview Avenue, Clayton 3168, Victoria, Australia
[§]School of Applied Sciences, RMIT University, 124 Latrobe Street, Melbourne 3001, Victoria, Australia
[∥]Energy Technology, CSIRO, Bayview Avenue, Clayton 3168, Victoria, Australia
[⊥]Japan Science and Technology Agency (JST), PRESTO, 4-1-8 Honcho Kawaguchi, Saitama 332-0012, Japan

Ⓢ *Supporting Information*

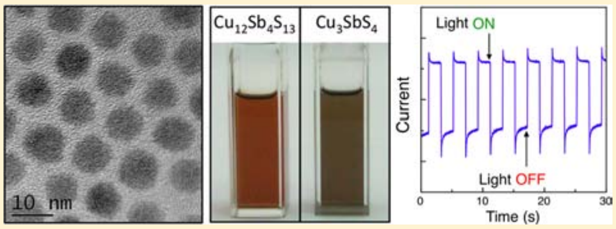

ABSTRACT: Herein, we present the novel synthesis of tetrahedrite copper antimony sulfide (CAS) nanocrystals ($Cu_{12}Sb_4S_{13}$), which display strong absorptions in the visible and NIR. Through ligand tuning, the size of the $Cu_{12}Sb_4S_{13}$ NCs may be increased from 6 to 18 nm. Phase purity is achieved through optimizing the ligand chemistry and maximizing the reactivity of the antimony precursor. We provide a detailed investigation of the optical and photoelectrical properties of both tetrahedrite ($Cu_{12}Sb_4S_{13}$) and famatinite (Cu_3SbS_4) NCs. These NCs were found to have very high absorption coefficients reaching 10^5 cm^{-1} and band gaps of 1.7 and 1 eV for tetrahedrite and famatinite NCs, respectively. Ultraviolet photoelectron spectroscopy was employed to determine the band positions. In each case, the Fermi energies reside close to the valence band, indicative of a p-type semiconductor. Annealing of tetrahedrite CAS NC films in sulfur vapor at 350 °C was found to result in pure famatinite NC films, opening the possibility to tune the crystal structure within thin films of these NCs. Photoelectrochemistry of hydrazine free unannealed films displays a strong p-type photoresponse, with up to 0.1 mA/cm^2 measured under mild illumination. Collectively these optical properties make CAS NCs an excellent new candidate for both thin film and hybrid solar cells and as strong NIR absorbers in general.

■ INTRODUCTION

Semiconductor nanocrystals (NCs) show great promise for their use as the active absorbers in photovoltaic devices,[1−3] thin-film thermoelectrics,[4,5] and transistors.[6] With a focus on such nanocrystal-based devices, recent research has been directed toward the production of solution processable semiconducting colloids, which permit the active layers of various devices to be literally printed at a comparatively low cost as compared to other methods.[6−8]

Of particular interest has been the synthesis of semiconductor NCs for photovoltaic applications. In an effort to find new materials with physical properties appropriate for photovoltaics, the field of NC synthesis, which has been dominated by the characterization of binary semiconductor systems, has recently expanded to explore more complex ternary and quaternary structures. Sparked by the success of bulk copper indium gallium diselenide (CIGS) solar cells produced using chemical bath deposition methods,[9] $CuInS_2$,[10] $CuInSe_2$,[11] and $CuIn_xGa_{1-x}Se_2$[12] NCs have all been synthesized in recent years. However, concerns about the global availability of indium and gallium and their high cost have driven research into the synthesis of NCs for implementation in solar cells that utilize low-cost earth-abundant elements. In this regard, Cu_2ZnSnS_4,[13−16] Cu_2SnSe_3,[17] $Cu_2Zn_xSn_ySe_{1+x+2y}$,[18] Fe_2S,[19,20] Cu_2FeSnS_4,[21] and SnS[22] have all emerged as promising alternatives.

Despite these efforts, antimony-containing NCs have been largely overlooked. To date, there are only a few reports on such NCs. Colloidal $Pb_xSb_{2y}Te_{x+3y}$[23] and $AgPb_xSbTe_{x+2}$[24] nanocrystals and Sb_2Se_3[25] nanowires have been synthesized with a view to thermoelectric applications, while InSb[26] nanocrystals have recently emerged as tunable NIR absorbers and emitters. However, there has been very little evaluation of antimony-based nanocrystals for photovoltaics despite SILAR deposited nanocrystalline Sb_2S_3/TiO_2 hybrid solar cells having already yielded efficiencies close to 7%.[27,28] These preliminary explorations into antimony-based sensitizers for solar photovoltaics are extremely promising.

The ternary I−V−VI semiconductor, copper antimony sulfide (CAS), is a p-type semiconductor with a direct bulk band gap in the NIR, which varies between ∼1 and 1.8 eV depending on the crystal structure.[29−35] CAS typically has a high absorption coefficient with values up to 4 × 10^5 cm^{-1} measured for bulk $CuSbS_2$.[35] Bulk CAS is comprised of cheap, readily available, and comparatively abundant elements, making

Received: March 16, 2013
Published: July 23, 2013

it a sustainable material for semiconductor-based device applications and a particularly attractive candidate for solar photovoltaics.

Despite these advantageous properties, investigations into the synthesis of CAS NCs are scarce, with reports emerging only recently on the synthesis of Cu_3SbS_4 (famatinite) nanocrystals[36] and $CuSbS_2$ (chalcostibite) nanobricks.[37] To the best of our knowledge, there have been no previous reports on $Cu_{12}Sb_4S_{13}$ (tetrahedrite) NCs. Furthermore, prior investigations into CAS NCs focused mainly on outlining the synthetic method necessary to produce the NCs. There have been no previous investigations into the ligand chemistries involved in the nucleation and growth of CAS NCs in general or any detailed account of their optical and electronic properties.

Here, we present for the first time the synthesis of tetrahedrite $Cu_{12}Sb_4S_{13}$ nanocrystals. The synthetic conditions necessary to achieve nearly monodisperse nanocrystals of various sizes are discussed, and their optical properties are presented. Investigations into the effects of the reaction conditions necessary to produce phase pure tetrahedrite NCs are outlined. The growth mechanism of tetrahedrite NCs and CAS NCs in general is then discussed. We provide a detailed investigation of the optical and electronic properties of both tetrahedrite ($Cu_{12}Sb_4S_{13}$) and famatinite (Cu_3SbS_4) NCs. Furthermore, data are presented on how to alter the band gap and crystal structure of these materials by adjusting the sulfur content during a film annealing process. Finally, the photoelectrochemical properties of thin films of these novel materials are presented.

■ RESULTS AND DISCUSSION

Synthesis and Characterization of $Cu_{12}Sb_4S_{13}$ Nanocrystals. Briefly, to synthesize monodisperse 9 nm tetrahedrite CAS nanocrystals (see Figure 1B), copper(I) chloride (0.56 mmol) and antimony(III) chloride (0.56 mmol) were heated with oleylamine (OLA), oleic acid (OA), and 1-octadecene (ODE) to 190 °C in an inert atmosphere. At this temperature, bis(trimethylsilyl)sulfide (0.31 mmol) was swiftly injected after which the reaction was allowed to cool to room temperature. Upon injection, the reaction solution immediately turned dark brown/black indicating the rapid nucleation of the CAS NCs. The as-prepared nanocrystals were then washed several times with chloroform and methanol. Details of the purification procedure and the methods employed to obtain tetrahedrite nanocrystals of different sizes are outlined in the Experimental Section.

Electron microscopy was performed to characterize the morphology of the nanocrystals. Figure 1A–D shows a series of transmission electron microscope (TEM) images of the purified CAS nanocrystals without size sorting. Panels A, B, and C show images of 6.4 ± 0.6 nm (σ = 9.3%), 8.8 ± 0.9 nm (σ = 10.1%), and 17.8 ± 1.8 nm (σ = 10.1%) CAS nanocrystals, respectively. The calculated percent numerical standard deviations are given in brackets. All of the synthesized nanocrystals have standard deviations around 10%, which is considered typical for monodisperse nanocrystals. Panel F shows the size distributions of the CAS nanocrystals from panels A–C. These distributions we collected on no less than 100 individual nanocrystals and subsequently used to calculate the statistics of the distributions. The insets highlight the morphology of the nanocrystals. While the smaller NCs are seen to be highly spherical, clear faceting of the largest size nanocrystals is observed, likely due to the reduced surface energy of certain crystal planes as the NCs approach bulk. Panel D shows a high-resolution image of a single 8.5 nm nanocrystal from panel B. The lattice fringes are clearly visible, highlighting the crystalline nature of the NCs. A high-resolution scanning electron microscope (SEM) image of a drop-cast film of the largest CAS NCs is shown in panel E. The SEM micrograph confirms the spherical morphology of the NCs and rules out disk shapes, which are common to some copper-based NCs.[10,38,39] Energy-dispersive X-ray spectroscopy of these particles confirmed their composition showing the presence of copper, antimony, and sulfur from the nanocrystals as well as carbon and oxygen from the ligands and trace amounts of residual chlorine from the precursors (see Supporting Information Figure S1).

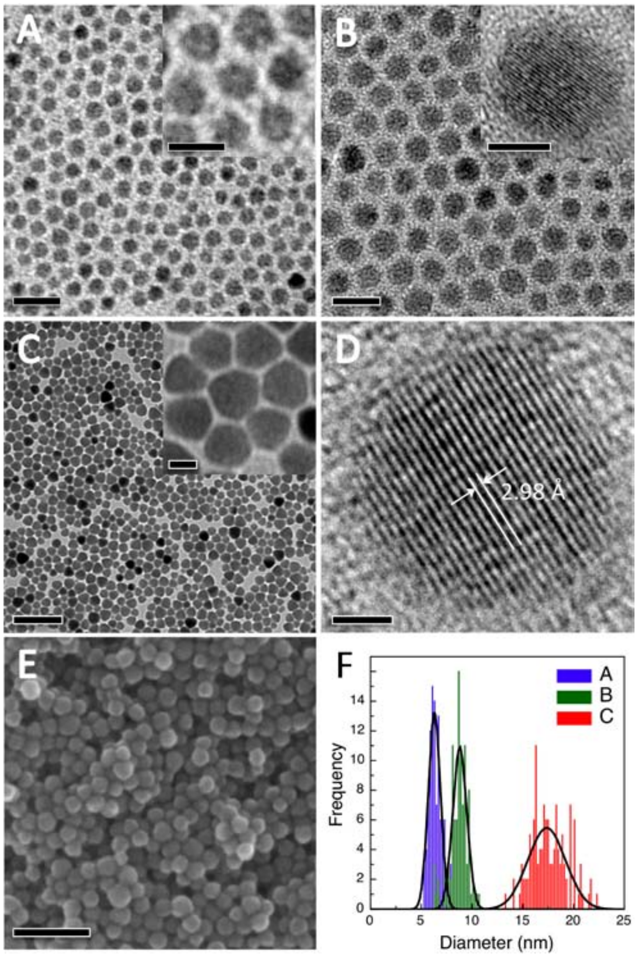

Figure 1. Electron microscope images of purified tetrahedrite CAS nanocrystals. The CAS nanocrystals are seen to be both monodisperse and crystalline. The sizes of the NCs are 6.4 ± 0.6 nm (σ = 9.3%), 8.8 ± 0.9 nm (σ = 10.1%), and 17.8 ± 1.8 (σ = 10.1%) for panels A–C, respectively. The scale bars for panels A–E (insets) are 20(10), 20(5), 100(10), 2, and 100 nm, respectively. Panel F shows the size distribution histograms gathered from panels A–C. All of the synthesized nanocrystals have standard deviations (σ) around 10%.

X-ray diffraction (XRD) was employed to determine the crystal phase of the nanocrystals. Figure 2 shows XRD patterns of the small (6.4 nm), intermediate (8.8 nm), and large (17.8 nm) nanocrystals investigated in this work. The CAS nanocrystals are an excellent match to the tetrahedrite ($Cu_{12}Sb_4S_{13}$) pattern (ICDD no. 00-024-1318). From

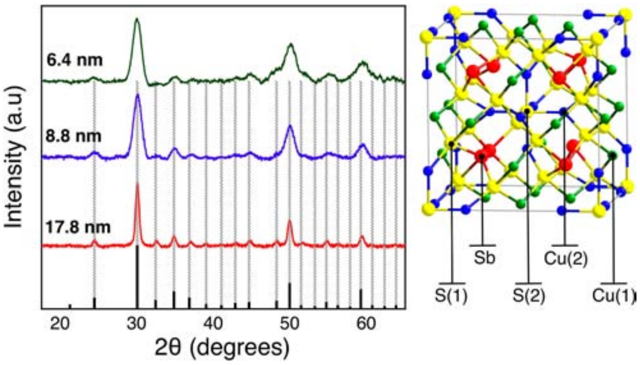

Figure 2. (Left) X-ray diffraction patterns of different sized tetrahedrite CAS nanocrystals. In all cases, the XRD patterns are an excellent match to the reflections of bulk tetrahedrite copper antimony sulfide (ICDD no. 00-024-1318). The vertical dotted lines serve to aid in the peak assignments. A clear broadening of the peaks is observed, which is consistent with a reduction in the size of the NCs. (Right) A single unit cell of tetrahedrite CAS highlighting the nature of the bonding in the NCs. For additional clarity, an enlarged version is available in the Supporting Information (Figure S2).

inspection of the XRD patterns, we can clearly see that both the weak and the strong reflections become broader as the particle size gets smaller, consistent with smaller crystal domains. From smallest to largest, the sizes of the nanocrystals calculated from the Debye−Scherrer formula using the main (222) lattice reflection at 29.9° 2*θ* are 7.54, 8.02, and 16.93 nm, respectively. These sizes are in excellent agreement with the TEM results and highlight the quality of the XRD patterns.

$Cu_{12}Sb_4S_{13}$ crystallizes as a body centered cubic lattice with an *I*43*m* space group (a = 10.33 Å). Tetrahedrite CAS is a slightly sulfur-rich (∼2 mol %) crystal of stoichiometric skinnerite (Cu_3SbS_3). A simulated image of a single unit cell of tetrahedrite CAS constructed using CrystalMaker 8.5.3 is seen in Figure 2. Because of its unusual stoichiometry, it contains two types of copper atoms either tetrahedrally (Cu(1)) or triangularly (Cu(2)) coordinated to sulfur as well as two types of sulfur atoms. S(1) is trigonally coordinated to three copper atoms and a single antimony atom, while S(2) is octahedrally coordinated to only copper. The antimony atoms are trigonally coordinated to S(1).[40]

Additional structural characterization can be gleaned from examination of Figure 1D, which shows a high-resolution TEM of a single $Cu_{12}Sb_4S_{13}$ nanocrystal. The lattice spacing was measured to be 0.298 nm. This value matches extremely well to the lattice spacing of the (222) lattice plane of bulk Cu_3SbS_3.[41]

Effect of Reaction Conditions. The reaction temperature as well as the types and concentrations of precursors and ligands had to be optimized to achieve phase pure, nearly monodisperse copper antimony sulfide NCs. Multiple different ligands were trialled as prospective passivants and precursors (see the Supporting Information for details). However, only a combination of amines and carboxylic acids was found to give the conditions necessary for both good nucleation and growth. Other ligand moieties likely bonded too strongly to copper and antimony to permit facile nucleation, resulting in the precipitation of bulk material upon injection. As such, oleylamine (OLA) and oleic acid (OA) or octanoic acid (OTA) were chosen for their ability to dissolve the metal chlorides. Given that $SbCl_3$ has a very low affinity to OLA and CuCl is unable to dissolve in OA within the temperature range investigated, here we hypothesize that the metal precursors are Cu(OLA) and $Sb(OA)_3$ or $Sb(OTA)_3$.[36]

Likewise, multiple sulfur precursors were also examined (see the Supporting Information for details). Of these precursors, only bis(trimethylsilyl)sulfide (TMS) was found to reproducibly give nanocrystalline copper antimony sulfide. Other forms of sulfur were either found to be not reactive enough to induce rapid nucleation or resulted in a bulk red/brown precipitate upon injection or heating, which likely contained large amounts of amorphous Sb_2S_3 or Sb_2S_5.[42,43] Given the nature of the precursors employed, here we expect that the initial pathway to NC formation involves the reaction of a metal ligand complex (MX_y) with $((CH_3)_3Si)_2S$ to form a M−S covalent bond with the elimination of $(CH_3)_3SiX$ through a dehalosilylation-type reaction mechanism.[44,45]

In the context of having chosen the ligand chemistries and precursors that resulted in the reproducible formation of CAS NCs, we then investigated the effect of precursor ratios. The concentrations of both antimony and sulfur were found to be critical to achieving phase pure samples. Considering the 3:1 elemental ratio of Cu:Sb in tetrahedrite CAS, the use of a stoichiometric 3-fold excess of antimony over copper (Cu:Sb, 1:1) was found to be necessary to completely avoid the nucleation of free copper sulfide NCs.

During a series of trial reactions, the amount of injected sulfur was also varied. For mole ratios of metal (M) to sulfur (S) within the range 1:0.25 to 1:0.5, pure tetrahedrite CAS nanocrystals are formed. Within this range, higher sulfur concentrations produce larger particles. Large excesses of sulfur are known to promote the formation of famatinite Cu_3SbS_4 NCs, with M:S ratios above 1:1.25 resulting in pure Cu_3SbS_4 NCs.[36] Reducing the sulfur content below 1:0.25 (M:S) resulted in the formation of an antimony sulfide impurity phase. This is highlighted in Figure 3A, which shows the XRD patterns of both the control reaction (method used to produce ∼9 nm CAS NCs; M:S, 1:0.25) and the same reaction conducted with low sulfur (1:0.15). It is seen that in the low sulfur limit the reaction results in the formation of Sb_2S_3 (ICDD no. 00-002-0374) in addition to $Cu_{12}Sb_4S_{13}$ as exemplified by the additional peaks indicated by the star markers.

In addition to optimizing the precursor chemistries, the nucleation and growth of CAS NCs was found to be extremely sensitive to the reaction temperature. Injection temperatures in excess of 210 °C resulted in uncontrolled growth of the nacent crystallites, while temperatures lower than 175 °C were insufficient to induce rapid nucleation. Reactions performed with injection temperatures of 150 and 170 °C resulted in the formation of highly polydisperse samples beginning from very small sizes, which is indicative of poor nucleation (see Supporting Information, Figure S3). These samples also indicated the presence of copper sulfide phases, which is direct evidence that the decomposition of the antimony precursor employed is not facile at temperatures below 180 °C.

Given the narrow temperature range required to form CAS NCs, no size tunability could be achieved by altering the injection temperature. Further attempts to adjust the growth kinetics of the NCs by altering the overall precursor concentrations, while perturbing the reaction kinetics and increasing the polydispersity of the samples, were found to have little effect on the overall average size of the nanocrystals. To tune the size of the nanocrystals, it was found to be necessary to carefully tune the ligand chemistry. As compared to the control reaction, the substitution of oleic acid for octanoic acid, using a

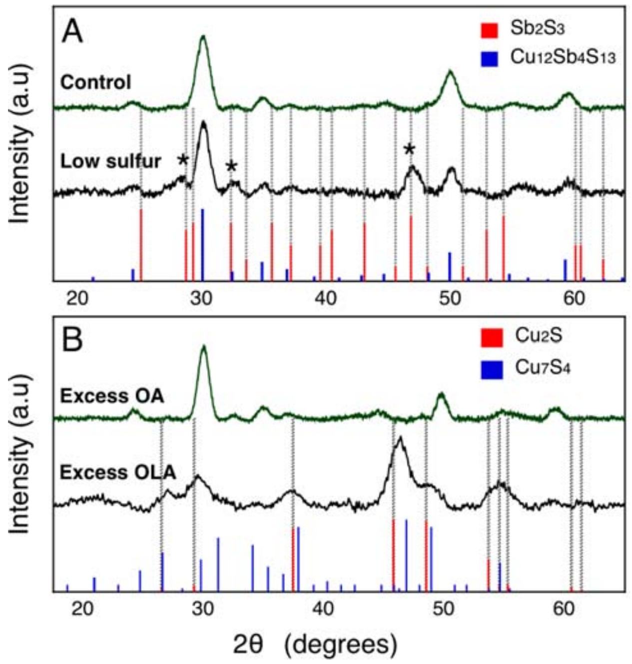

Figure 3. X-ray diffraction of tetrahedrite CAS nanocrystals produced under various reaction conditions. (A) The control reaction and the same reaction with a 50% reduction in sulfur, which causes the formation of an Sb_2S_3 contaminant phase. (B) XRD patterns of the control reaction for CAS with a 2-fold excess of oleic acid (OA) or oleylamine (OLA). While OA preserved the phase purity, OLA promotes the formation of copper sulfide species.

slightly higher growth temperature (200 °C), and increasing the sulfur content resulted in larger CAS NCs (Figure 1C). As all of the reactions performed here are conducted with an excess of metal precursors, increasing the sulfur content promotes further growth in the later stages of the reaction. Additionally, shorter chain ligands are known to facilitate the growth of larger NCs as they are more dynamic at the NC surface for a given temperature.[46] Contrary to what is commonly observed,[47,48] increasing the amounts of both OLA and OA (overall ligand concentration) was found to produce smaller CAS NCs (Figure 1A). As such, it is clear that for the CAS reaction system increasing concentrations of OLA and OA have a minimal effect on the level of supersaturation (precursor solubility) that governs the nucleation stage.

Further experiment revealed that not only the overall ligand concentration (and chain length) but also the relative concentrations of the ligands were of great importance. Figure 3B shows the XRD patterns of NCs produced in both excess OLA and excess OA. Reactions conducted with a 2-fold excess of OLA over OA almost completely suppressed the formation of $Cu_{12}Sb_4S_{13}$ and promoted the formation of free copper sulfide species. Both β-Cu_2S (ICDD no. 00-026-1116) and Cu_7S_4 (ICDD no. 00-023-0958) dominate the XRD patterns of NCs synthesized with excess OLA. The fact that amines promote the nucleation of copper sulfide phases is consistent with the ubiquitous use of amines in the syntheses of copper sulfide NCs.[49−52] Conversely, the use of excess OA preserved the formation of $Cu_{12}Sb_4S_{13}$ NCs, although the particles were seen to become slightly more polydisperse and faceted. From these results, it is clear that a fine balance between amines and carboxylic acids is necessary to achieve monodisperse CAS nanocrystals without impurities. TEM images of the particles produced from varying the precursor ratios and ligand concentrations may be viewed in the Supporting Information (Figure S4).

To explain the observation that increased ligand concentrations result in smaller CAS NCs, we hypothesize the ligands primarily act to (1) stabilize the initial nuclei by reducing their surface energy, thus promoting nucleation; or (2) increase the solubility of the precursors enough to limit the NC growth rate. If supposition (2) were dominant, then the increased ligand concentrations would result in a reduction in the supersaturation at both the nucleation and the growth stages. In such instances, the resultant suppression in the nucleation rate would increase the overall NC size, contrary to what is observed here. Further, the observation that higher amine concentrations promote the nucleation of copper sulfide is consistent only with supposition (1). Such “nucleating agents” have been explored previously.[47] From these data, we propose that the growth mechanism of CAS NCs is primarily dominated by the surface−ligand interactions and not through the dynamic solubility of the precursors in solution.

Interestingly, using the optimized reaction conditions without antimony chloride results in the nucleation of quite monodisperse copper sulfide NCs (see Supporting Information, Figure S5). Conversely, the same reaction without copper does not form crystalline Sb_2S_3 but rather instantly forms a bulk red powder (either amorphous Sb_2S_3 or Sb_2S_5).[42,43] This has important consequences, as in the absence of a dominant pathway to antimony sulfide clusters (or NCs), Cu−S bond formation becomes a prerequisite for CAS NC evolution. In this case, the rate of Cu−S bond formation dictates the nucleation rate of the CAS nanocrystals. Similar observations have been made previously for CIS nanorods[53] and CIGS NCs.[54]

In summary, to realize phase pure CAS NCs, the overall availability of antimony must be maximized. This is achieved by using high enough temperatures (to kinetically favor disassociation of the antimony precursor) and the presence of OA (to thermodynamically stabilize the antimony atoms on the surface of the growing nuclei). Likewise, the nucleation of copper sulfide must be minimized, which is achieved through the use of low amine concentrations. In this way, the rate of antimony incorporation into the primordial lattice occurs at a rate comparable to free copper sulfide formation, culminating in the growth of a ternary lattice. Such a mechanism is consistent with the need for a high Sb:Cu mol ratio required in the reactions conducted here. This is in sharp contrast to CZTS,[14,55,56] CIS(Se),[10,11,57] and CIGS[12] NC formation, which can be conducted in near pure amine with stoichiometric quantities of monomers.

Optical Properties. Figure 4A shows the absorption spectra of the three sizes of tetrahedrite CAS NCs investigated here in tetrachloroethylene. The spectra were all normalized at 670 nm (local minimum) for clarity. It can be seen that all of the NCs, regardless of size, have a strong absorption at higher energies that approaches a minimum at approximately the same energy. Analysis of the band gaps using Tauc plots of the form $Ah\nu^n$ was performed (see Supporting Information, Figure S6). The most linear spectra were observed for $n = 1/2$, indicative of an indirect band gap material. Indirect band gaps at 1.80, 1.78, and 1.69 eV were extrapolated for CAS NCs with average diameters of 6.4, 8.8, and 17.8 nm, respectively. These values agree well with the measured bulk band gap of tetrahedrite at 1.72 eV.[58] It is important to note here that for other copper-

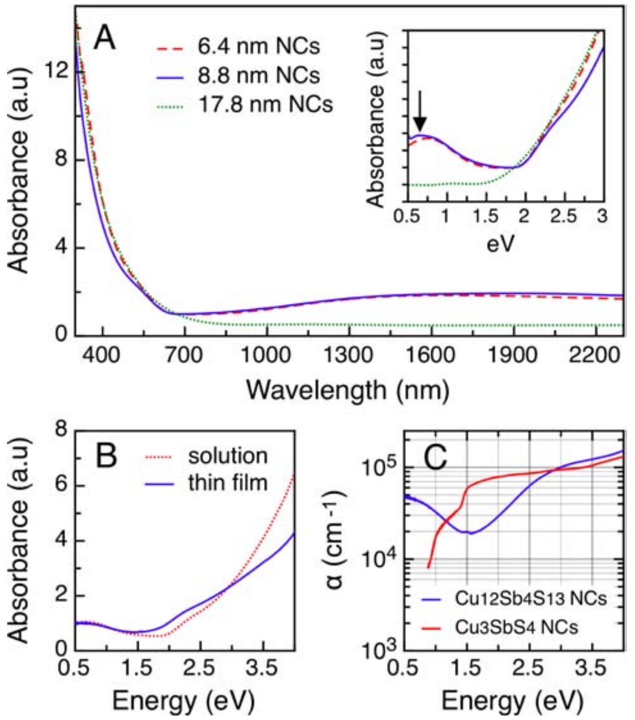

Figure 4. (A) Absorption spectra of different sized tetrahedrite CAS NCs in tetrachloroethylene. The same spectra on an electronvolt scale highlighting the band extending to lower energies for the smaller sized NCs (inset). (B) Comparison of the solution and film spectra for $Cu_{12}Sb_4S_{13}$ NCs normalized at 0.5 eV. (C) Absorption coefficient of ~9 nm $Cu_{12}Sb_4S_{13}$ and ~10 nm Cu_3SbS_4 NCs. The absorption coefficients are seen to be greater than 10^4 cm^{-1} over the entire visual region, reaching 10^5 cm^{-1} over 3 eV.

based semiconductors, such as Cu_2ZnSnS_4,[59,60] $Cu_{2-x}S$,[61] and $CuInSe_2$,[62] band gap tunability is only observed for sizes below around 5−6 nm. As such, we cannot rule out the possibility of quantum size effects becoming prevalent for ultrasmall tetrahedrite CAS NCs.

Further inspection of the absorption spectrum reveals that for all NC sizes the absorbance is nonzero over the range of energies probed. Interestingly, while the larger NCs have a flat nonzero absorbance between ca. 800−2300 nm, which is similar to reports on bulk tetrahedrite,[58] the smaller tetrahedrite CAS NCs have a distinct broad band that extends from around 800 nm to lower energies. This band is more easily identifiable on an electronvolt scale, as shown in the inset of Figure 4A (see arrow).

The appearance of such a band, although common in the emission spectra (due to midband gap trap states[63]), is not typically observed in the absorbance spectra of semiconductor NCs. In the case of $Cu_{2-x}S$ NCs, the presence of such a band is observed and has been attributed to a (localized surface) plasmon resonance (LSPR)[61,64] (see Supporting Information, Figure S5). As such, it is reasonable to consider that the origin of the NIR absorption band may also be due to a LSPR.

A definitive method to determine whether the band is plasmonic in origin (or has plasmonic character) is to test the sensitivity of the absorption band to solvents of different refractive indices. Absorption bands with strongly plasmonic character are known to red shift with increasing refractive index.[61] Absorption measurements of ~9 nm CAS NCs revealed the position of the NIR band to be completely insensitive to solvents with refractive indices between 1.46 and 1.63 (see Supporting Information, Figure S7). Given these data, we may rule out the possibility that the NIR band possesses plasmonic character. This conclusion is consistent with the fact that an LSPR mode should be dampened for small particle sizes due to scattering, contrary to what is observed. As such, we confidently attribute the broad NIR absorption band to the presence of midband gap states, which possess significant oscillator strength.

Charge neutrality in tetrahedrite is achieved through the inclusion of $Cu^{(II)}$ (or other divalent elements). General structures of the form $Cu^{(I)}{}_{10-x}Cu^{(II)}{}_{x}Sb^{(III)}{}_{4}S^{(2-)}{}_{13}$ have been measured with $Cu^{(II)}$:$Cu^{(I)}$ ratios as high as 1:14.[65,66] X-ray photoelectron spectra of bulk tetrahedrite, synthesized via solvothermal methods,[67] as well as the CAS NCs reported here clearly showed the presence of two distinct copper cations (charge environments) as well as broad "shake up" bands, which confirmed the presence of $Cu^{(II)}$[68,69] (see Supporting Information, Figure S8). Given the absence of a broad NIR band for famatinite CAS NCs[36] (which has a zero absorbance under the band gap and contains only $Cu^{(I)}$), it is highly likely that the states that give rise to the nonzero absorbance across the NIR region are strongly associated with the presence of $Cu^{(II)}$ atoms.

On the basis of the increased intensity of the NIR band in small CAS NCs, and given the fact that the optical properties of small NCs are increasingly dictated by the nature of the surface environment, it is probable that these $Cu^{(II)}$ states are somewhat surface localized. This is supported by XPS results, which confirmed the presence of higher ratios of $Cu^{(II)}$:$Cu^{(I)}$ in smaller CAS NCs as well as surface bound oxidation products such as $CuSO_4$ (see Supporting Information, Figure S8).

Figure 4B shows absorption spectra from both solution and a thin film (~35 nm) of 9 nm CAS NCs normalized at 0.5 eV. The two absorption spectra are nearly identical, highlighting the negligible scattering and high quality of the thin films fabricated for this work. Figure 4C displays the absorption coefficient as a function of photon energy calculated from a densely packed thin film of ~9 nm tetrahedrite and ~10 nm famatinite CAS NCs. The measured absorption coefficients of these NCs are seen to be greater than 10^4 cm^{-1} over the entire visual region reaching 10^5 cm^{-1} at energies greater than 3 eV. Such high absorption coefficients make CAS NCs attractive candidates for use as light harvesters in solar photovoltaic devices.

Tuning the Crystal Structure. Copper antimony sulphide has four common crystal phases: tetrahedrite ($Cu_{12}Sb_4S_{13}$), famatinite (Cu_3SbS_4), skinnerite (Cu_3SbS_3), and chalcostibite ($CuSbS_2$). A recent report by the authors outlines the novel synthesis of monodisperse famatinite NCs.[36] These NCs have the smallest band gap of all of the structures and may be synthesized by employing a method similar to that used to produce approximately 9 nm tetrahedrite CAS NCs but altering the reaction conditions and using an excess of sulfur. Famatinite NCs have a band gap of ~1 eV and also have high absorption coefficients approaching 10^5 cm^{-1} (see Figure 4C). A schematic summarizing how to achieve both tetrahedrite and famatinite crystal structures is outlined in Figure 5A. Colloidal solutions of famatinite and tetrahedrite are also shown. The dilute solutions serve to highlight the markedly different band gaps of the two crystal structures. For completeness, optical characterization of both the novel $Cu_{12}Sb_4S_{13}$ NCs as well as Cu_3SbS_4 NCs (recently synthesized by the authors) was conducted.

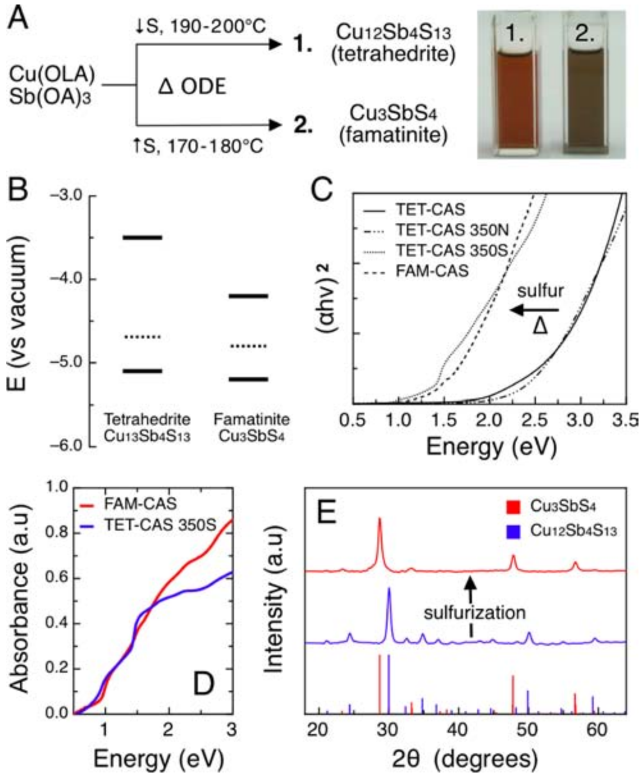

Figure 5. (A) Schematic outlining the changes in the reaction conditions required to synthesize either tetrahedrite or famatinite CAS NCs. (B) The band positions (solid lines) and Fermi energies (dotted lines) for both famatinite and tetrahedrite CAS NCs as determined by UPS. (C) Tauc plot ($n = 2$; direct) for tetrahedrite and famatinite films annealed under various conditions (350S = 350 °C in a sulfur atmosphere, 350N = 350 °C in a nitrogen atmosphere). (D) Raw spectra of as-prepared famatinite and sulfurized tetrahedrite films. The similarity between the sulfurized tetrahedrite film and the as-prepared famatinite film is clearly evident. (E) Thin film XRD patterns of tetrahedrite NC films before and after sulfurization. Complete conversion to the famatinite crystal structure is observed. Notably, no residual impurity phases could be detected.

To investigate the band structure of these novel materials, ultraviolet photoelectron spectroscopy (UPS) was used to establish the valence band and Fermi energies. The raw UPS spectra and corresponding analysis may be found in the Supporting Information (see Figure S10). From analysis of the UPS spectra and taking an average of the measured band gaps for $Cu_{12}Sb_4S_{13}$ at 1.7 eV and for Cu_3SbS_4 at 1 eV, we calculate the valence band (conduction band) edges at 5.1 eV (3.4 eV) and 5.2 eV (4.2 eV), respectively. Likewise, the Fermi energies of these two phases were determined to be 4.7 and 4.8 eV for $Cu_{12}Sb_4S_{13}$ and Cu_3SbS_4, respectively. The position of the Fermi level close to the valence band in both cases confirms the p-type nature of the two structures of CAS NCs investigated here.

Figure 5B shows a schematic of the band structure of tetrahedrite and famatinite NCs. Inspection of the band structure reveals that the valence band positions remain relatively constant between the two crystal structures. As such, band gap tunability is imparted almost solely through a decrease in the conduction band edge upon going from tetrahedrite to famatinite CAS NCs.

In the case of tetrahedrite, it is likely that the strong p-type character is imparted through either copper deficiencies in the lattice or the presence of $Cu^{(II)}$, which would result in valence band electron deficiencies[61] permitting greater carrier mobility within the valence band. The nature of the p-type character of famatinite cannot be attributed to either of these phenomenon as they do not contain $Cu^{(II)}$ nor do they possess an NIR absorption band consistent with copper vacancies. The weaker p-type character is thus most likely an intrinsic property of the crystal structure itself.

The NIR band gaps and the high absorption coefficients across the visible and NIR spectral regions make these NCs excellent light harvesters. In addition, the band and Fermi edge positions permit their use as potential donor or acceptor materials in a variety of sensitized solar cells,[27,70−72] as well as p-type semiconductors in inorganic thin film solar cell device architectures.

To further investigate the properties of these two crystal structures, we prepared thin films of both of these materials. Tauc plots of these films (for $n = 2$; direct) under various conditions are shown in Figure 5C. Annealing of the as-prepared tetrahedrite CAS NC films at 350 °C under nitrogen had little effect on the absorption spectrum. In sharp contrast, annealing of these films under the same conditions in a sulfur atmosphere resulted in a large shift in the absorption profile. First, the absorption shifted ∼700 meV to lower energies. Second, the absorption profile became more direct in nature as indicated by an increased linearity. It is important to note that copper antimony sulfides are direct band gap semiconductors in the bulk state.[29,31−34] Their indirect character in colloidal form is thus directly correlated with surface "dangling bonds" inherent to all nanocrystals. It is therefore not surprising that high temperature treatment of the films, which typically results in grain growth and the annealing of defects, culminates in increasing the direct character of the absorption transitions. Such observations have been made upon the annealing of colloidal Cu_2ZnSnS_4 nanocrystal thin films.[73]

Upon further inspection of Figure 5C, it is seen that the absorption spectra of the sulfurized tetrahedrite film (TET-CAS 350S) appear almost identical to those of the as-prepared unannealed famatinite CAS NC film (FAM-CAS). The raw spectra of both sulfurized tetrahedrite and as-prepared famatinite are shown in Figure 5D for clarity (see also Supporting Information S9). Given the clear similarities in these spectra and the fact that famatinite is a sulfur-rich version of tetrahedrite, we propose that sulfurization of the tetrahedrite NC film results in a change in crystal structure. To confirm this hypothesis, thin film XRD was performed on the as-prepared tetrahedrite films before and after sulfurization. Examination of Figure 5E reveals that sulfurization of the tetrahedrite NC film resulted in complete conversion to the famatinite crystal structure without any residual impurity phases. This phenomenon permits easy access to thin films of both crystal structures. In addition, it opens up the possibility of tuning the conduction band position (and band gap) simply by controlling the extent of sulfurization within the NC film.

Photoelectrochemistry. To test the photoresponse of CAS NCs, thin films of both 9 nm tetrahedrite and 10 nm famatinite NCs were spin-cast onto ITO substrates (see the Experimental Section for details). Surface profilometry of the thin films showed thicknesses of ∼65 nm for both the tetrahedrite and the famatinite films investigated here. These films were mounted to a custom built three-electrode photoelectrochemical cell with a coiled Pt wire working electrode and an AglAgCl reference electrode containing an aqueous Eu^{3+} electrolyte as an electron acceptor. Europium(III) was chosen as it has a reduction potential energetically below the conduction band edge of both materials to enable photoreduction and does not absorb light at the probe wavelength.

In general, photoelectrochemical characterization is an excellent tool to reliably evaluate the photoresponse of a semiconductor film (of different types and morphologies) without the complications associated with additional contacts. Further, in such thin film electrochemical cells the distance the minority carriers (in this case, electrons) must travel is minimized, which reduces their probability to recombine with photogenerated holes.

Figure 6 shows the current−voltage curves under pulsed blue LED illumination for as-prepared (unsintered) tetrahedrite (upper panel) and famatinite (lower panel) NC films. In both cases, the photocathodic current increases with increasing negative bias, which is indicative of a p-type film. The photocurrents for both CAS NC films are seen to increase significantly with increasing negative bias reaching up to ∼0.06 mA cm^{-2} at −0.4 V and ∼0.1 mA cm^{-2} at −0.5 V for tetrahedrite and famatinite films, respectively. From analysis of the *JV* curves, it is seen that the CAS NC films respond rapidly to illumination, with peak-to-peak switching occurring on millisecond time scales.

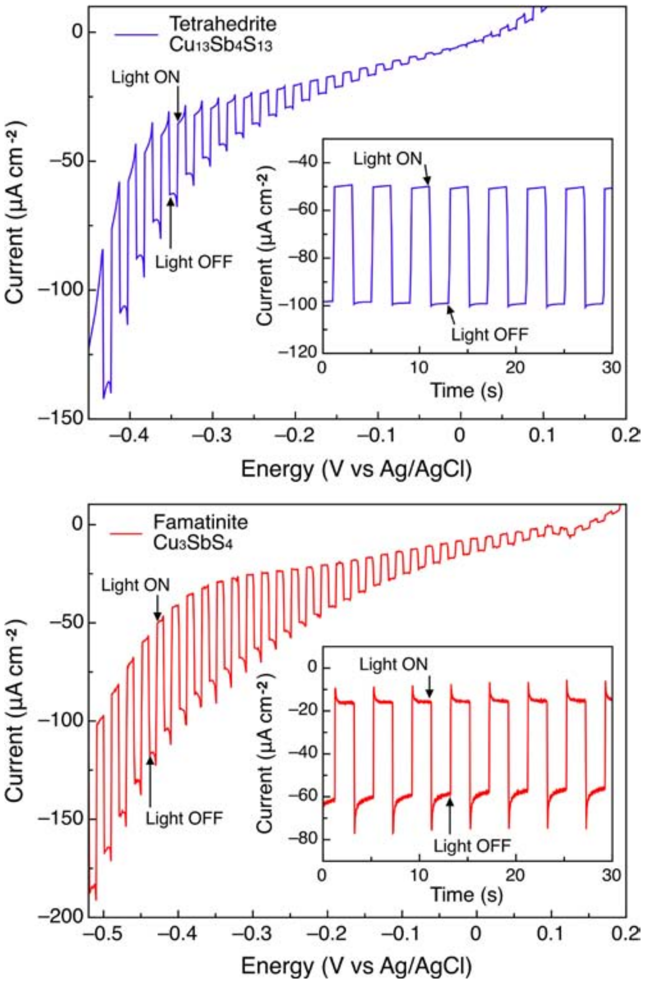

Figure 6. Current−voltage curves for tetrahedrite (upper panel) and famatinite (lower panel) NC films conducted at a scan rate of 10 mV s^{-1}. The insets show the photoresponse under pulsed illumination (2 s ON/OFF) at a constant potential of −0.4 V. In contrast to the square wave response seen for the tetrahedrite film, clear peaks are observed for the famatinite films.

In the case investigated here, the CAS NC film under illumination transfers electrons to the Eu^{3+} (reducing it to Eu^{2+}), and an electron is transferred from the back ohmic contact at the ITO/CAS interface into the CAS NC film. We see for both cases a rapid increase in dark current at potentials approaching −500 meV, which is caused by the direct reduction of Eu^{3+} to Eu^{2+} whose reduction potential is −550 meV vs Ag| AgCl.

To evaluate the response of the films independent of a changing potential, constant voltage experiments were performed. Such experiments enable a more realistic evaluation of the charge transport dynamics for device applications, which operate at a constant internal field. The insets show the photoresponse of both films subjected to 2 s ON/OFF cycles at a constant potential of −0.4 V over 30 s. The peak-to-peak photocurrents are seen to be extremely stable. Stability studies of the films over longer time scales were conducted and are reported in the Supporting Information (see Figure S11). From inspection of the insets of Figure 6, differences in the charge transport dynamics between the two crystal structures are clearly evident. Contrary to the square wave response seen for the tetrahedrite films, the famatinite films have a transient photocurrent decay component. As these experiments were performed at low light intensities (∼1.8 mW) and with high Eu^{3+} concentrations (0.125 M), it is highly unlikely that the peaks observed in the films are due to limited charge (minority carrier) dissipation at the CAS−electrolyte interface. Furthermore, similar dynamics were consistently observed for multiple different films of both tetrahedrite and famatinite CAS NCs. Thus, we propose that the observed dynamics are representative of the types of NCs employed here.

These preliminary results on the photoresponse of CAS NC films are very encouraging and are competitive with the dynamics observed for thin films of other well established[73−75] and highly novel NC materials.[17,21,37,76] Notably, the CAS NC thin films investigated here were prepared without a high temperature heat treatment step or the use of hydrazine, both of which are known to greatly improve the photoresponse and conductivity of semiconductor films.[15,73,77−80] Additional optimization of film thickness, NC surface chemistry, as well as the type of electrolyte is expected to result in further improvements to the photocurrents.

■ CONCLUSIONS

The synthesis of tetrahedrite CAS NCs has been reported for the first time. Using the developed synthetic method, CAS nanocrystals with sizes between 6 and 18 nm can be obtained. Excess antimony and low amine concentrations were found to be necessary to achieve phase pure samples. From XPS and optical analysis, we attribute the unusual NIR absorption band present for $Cu_{12}Sb_4S_{13}$ NCs to the presence of $Cu^{(II)}$ in the crystal lattice.

Detailed optical and photoelectrochemical characterization of both the novel $Cu_{12}Sb_4S_{13}$ NCs as well as Cu_3SbS_4 NCs was conducted. Both crystal structures were found to have high absorption coefficients reaching 10^5 cm^{-1}. Indirect band gaps for Cu_3SbS_4 and $Cu_{12}Sb_4S_{13}$ were measured at ∼1 and ∼1.7 eV, respectively, which were seen to become more direct in character upon high temperature annealing. The markedly different band gaps of these two related crystal structures can be attributed almost solely to a shift in the conduction band position. We have demonstrated the ability to switch the band gap between 1.7 and 1 eV in dependence upon the annealing conditions of the thin films. Using thin film XRD, we have unambiguously linked these optical changes to a change in crystal structure. Photoelectrochemistry of these films revealed rapid response to pulsed illumination and promising initial photocurrents reaching 0.1 mA cm^{-2} for hydrazine free unannealed films under mild illumination.

Collectively, their NIR band gaps, deep valence band positions, high absorption coefficients, as well as their p-type photoresponse make $Cu_{12}Sb_4S_{13}$ and Cu_3SbS_4 attractive candidates for application in photovoltaic devices of different architectures as well as strong NIR absorbers in general.

■ EXPERIMENTAL SECTION

Materials. Antimony(III) chloride (>99%), copper(I) chloride (>99.995%), sulfur powder (99.98%), oleic acid (90%), octanoic acid (98%), oleylamine (70%), octylamine (99%), bis(trimethylsilyl)sulfide (synthesis grade), 1-octadecene (90%), trioctylphosphine (90%), trioctylphosphine oxide (90%), dodecanethiol (>98%), 1-octanol (>99%), tetrachloroethylene (≥99%), chlorobenzene (99.9%), and europium(III) chloride hexahydrate (99.9%) were procured from Sigma Aldrich. *N*-Hexylphosphonic acid (>99%, PCI synthesis), bis(2,4,4-trimethylpentyl)phosphinic acid (Cytec Industries), carbon disulfide (99.9%), acetone (99.5%), ethanol (99.5%), methanol (99.5%), ether (99.5%), and chloroform (99.8%) were purchased from Merck. ITO glass was purchased from Samsung Corning (185 ± 20 nm, 8.5 ± 1.5 Ω/□). FTO glass was purchased from Dyesol (TEC8, 8 Ω/□). All chemicals and solvent were used as received.

General Instrumentation. Absorption measurements were conducted using a JASCO V-670 spectrophotometer. XRD was performed on a Bruker D8 Discover microdiffractometer fitted with a GADDS (General Area Detector Diffraction System). Data were collected at room temperature using Cu Kα radiation (λ = 1.54178 Å) with a potential of 40 kV and a current of 40 mA, and filtered with a graphite monochromator in parallel mode (175 mm collimator with 0.5 mm pinholes). The samples were mounted vertically, and aligned on an XYZ stage with the aid of a camera and laser guide. UPS measurements were made on a Kratos Axis-HSi using He I radiation (21.2 eV). Samples were prepared on ITO glass and referenced to the Fermi edge of argon etched gold. On the basis of the spectral width of the Fermi edge, we place an upper resolution limit on the measurements to ±0.15 eV.

Electron Microscopy. Low-resolution images were taken on a Philips CM120 BioTWIN transmission electron microscope (TEM) operating at 120 keV. High-resolution TEM images were acquired using a Jeol 2100F TEM/STEM (2011) with an X-ray detector and a Gatan Image Filter operated at 200 keV. Strong carbon coated 300-mesh grids were employed, and all grids were cast from dilute dispersions of NCs in chloroform. Scanning electron micrographs and elemental analysis (EDAX) were performed by loading a drop-cast sample on an aluminum stub on a FEI Nova NanoSEM (2007) with EDAX Si(Li)X-ray detector.

Size Tuneability. *6 nm* $Cu_{12}Sb_4S_{13}$ *NCs (Figure 1A).* 0.056 g (0.56 mmol) of copper(I) chloride, 0.128 g (0.56 mmol) of antimony(III) chloride, 1.0 g (3.73 mmol) of oleylamine, 1.0 g (3.54 mmol) of oleic acid, and 4 g of 1-octadecene (ODE) were heated under vacuum at 110 °C for 30 min. At this time, the reaction was pump/purged three times with nitrogen, and the temperature was raised to 190 °C. At this time, the solution appeared slightly turbid and yellow. At this temperature, 65 μL (0.31 mmol) of TMS in 1 g of ODE was swiftly injected, after which the reaction was removed from the heat and then allowed to cool to room temperature under constant stirring.

9 nm $Cu_{12}Sb_4S_{13}$ *NCs (Control Reaction; Figure 1B).* 0.056 g (0.56 mmol) of copper(I) chloride, 0.128 g (0.56 mmol) of antimony(III) chloride, 0.5 g (1.87 mmol) of oleylamine, 0.5 g (1.77 mmol) of oleic acid, and 5 g of 1-octadecene (ODE) were heated under vacuum at 110 °C for 30 min. At this time, the reaction was pump/purged three times with nitrogen, and the temperature was raised to 190 °C. At this temperature, 65 μL (0.31 mmol) of TMS in 1 g of ODE was swiftly injected, after which the reaction was removed from the heat and then allowed to cool to room temperature under constant stirring.

18 nm $Cu_{12}Sb_4S_{13}$ *NCs (Figure 1C).* 0.056 g (0.56 mmol) of copper(I) chloride, 0.128 g (0.56 mmol) of antimony(III) chloride, 0.5 g (1.87 mmol) of oleylamine, 0.5 g (3.46 mmol) of octanoic acid, and 5 g of 1-octadecene (ODE) were heated under vacuum at 110 °C for 30 min. At this time, the reaction was pump/purged three times with nitrogen, and the temperature was raised to 200 °C. At this temperature, 128 μL (0.61 mmol) of TMS in 1 g of ODE was swiftly injected, after which the reaction was removed from the heat and then allowed to cool to room temperature under constant stirring.

Washing and Thin Film Preparation. To effectively purify the nanocrystals, it is necessary to first separate the unreacted salts. To accomplish this, the mother liquor (2 mL) was dispersed in hexane (5 mL), and acetone (0.3 mL) was then added. The mixture was then centrifuged at 3000 rpm for 10 min. After centrifugation, the excess salt precipitated as a white powder. It was found that the removal of the unreacted salts was critical to obtaining optically clear solutions. The supernatant was then isolated, chloroform (1 mL), methanol (5 mL), and acetone (2 mL) were added, and then the dispersion was centrifuged at 4000 rpm for 10 min to precipitate the NCs. The semi pure plug could then be purified by several precipitation/dispersion cycles using chloroform/methanol/acetone (1:1:2 v/v).

To generate the NC "ink" for thin film fabrication, the purified CAS NCs in chloroform were first ligand exchanged with octylamine and redispersed in chlorobenzene to a concentration of 100 mg/mL. *n*-Hexylphosphonic acid was then added (2 mg/mL), and the solution was sonicated for 10 min. The phosphonic acid is required to ensure complete dispersion of the NCs and also imparts colloidal stability at high weight fractions. Finally, the ink was filtered through a 0.20 μm RC-membrane filter (Whatman). Films were spun on ITO substrates (1000 rpm, 30 s), which were precleaned by consecutively sonicating the substrates in distilled water, acetone, and *n*-propanol for 5 min each. The films were then placed on a hot plate at 200 °C for 10 min inside a N_2 filled glovebox to ensure complete removal of the excess solvent.

Electrochemistry. Electrochemistry was performed on 60−80 nm films of tetrahedrite and famatinite CAS NCs on ITO. For details on the synthesis of 10 nm famatinite Cu_3SbS_4 NCs used in this investigation, the reader is referred elsewhere.[36] The films were fixed to a custom built electrochemical cell consisting of a coiled platinum working electrode and a Ag/AgCl reference electrode. The voltage of the cell was manipulated using a Powerlab 4/20 controlled using EChem software (ver. 1.5.2, AD Instruments). The light source consisted of a 455 nm blue LED (LUXEON "Royal Blue") equipped with a diffuser. The sample was illuminated through the ITO onto the back contact. The light intensity at the sample was measured using a Hamamatsu silicon photodiode (0.43 mA on 6.6 mm^2). The calculated light intensity from calibration curves yielded ~1.85 mW incident upon the photodiode corresponding to a total flux of ~28 mW cm^{-2}.

■ ASSOCIATED CONTENT

Ⓢ Supporting Information

Additional experimental and nanocrystal characterization, inclusive of EDAX, SEM, TEM, Tauc analysis, XPS, UPS, and photoelectrochemical stability tests. This material is available free of charge via the Internet at http://pubs.acs.org.

■ AUTHOR INFORMATION

Corresponding Author

joel.vanembden@csiro.au; yasuhiro.tachibana@rmit.edu.au

Present Address

[#]Materials Science and Engineering, CSIRO, Bayview Avenue, Clayton, Victoria 3168, Australia.

Notes

The authors declare no competing financial interest.

■ ACKNOWLEDGMENTS

We acknowledge funding support from the JST PRESTO program (Photoenergy Conversion Systems and Materials for the Next Generation Solar Cells), Jacek Jasienak for his help with the UPS, and Enrico Della Gaspera for additional help with XRD measurements. We also acknowledge Dr. Phil Francis and Prof. Dougal G. McCulloch (RMIT Microscopy & Microanalysis Facility, School of Applied Sciences, RMIT University) for access to TEM and SEM facilities.

■ REFERENCES

(1) Gur, I.; Fromer, N. A.; Geier, M. L.; Alivisatos, A. P. *Science* **2005**, *310*, 462.
(2) Kamat, P. V. *J. Phys. Chem. C* **2008**, *112*, 18737.
(3) Jasieniak, J.; MacDonald, B. I.; Watkins, S. E.; Mulvaney, P. *Nano Lett.* **2011**, *11*, 2856.
(4) Poudel, B.; Hao, Q.; Ma, Y.; Lan, Y.; Minnich, A.; Yu, B.; Yan, Z.; Wang, D.; Muto, A.; Vashaee, D.; Chen, X.; Liu, J.; Dresselhaus, M. S.; Chen, G.; Ren, Z. *Science* **2008**, *320*, 634.
(5) Wang, R. Y.; Feser, J. P.; Jong-Soo, L.; Talapin, D. V.; Segalman, R.; Majumdar, A. *Nano Lett.* **2008**, *8*, 2283.
(6) Ridley, B. A.; Nivi, B.; Jacobson, J. M. *Science* **1999**, *286*, 746.
(7) Frederik, C. K.; Jan, F.; Mikkel, J. *J. Mater. Chem.* **2010**, *20*, 8994.
(8) Chirila, A.; Buecheler, S.; Pianezzi, F.; Bloesch, P.; Gretener, C.; Uhl, A.; Fella, C.; Kranz, L.; Perrenoud, J.; Seyrling, S.; Verma, R.; Nishiwaki, S.; Romanyuk, Y.; Bilger, G.; Tiwari, A. *Nat. Mater.* **2011**, *10*, 857.
(9) Tokio, N.; Masayuki, M. *Jpn. J. Appl. Phys.* **2002**, *41*, 165.
(10) Kruszynska, M.; Borchert, H.; Parisi, J. R.; Kolny-Olesiak, J. *J. Am. Chem. Soc.* **2010**, *132*, 15976.
(11) Koo, B.; Patel, R.; Korgel, B. *J. Am. Chem. Soc.* **2009**, *131*, 3134.
(12) Panthani, M. G.; Akhavan, V.; Goodfellow, B.; Schmidtke, J. P.; Dunn, L.; Dodabalapur, A.; Barbara, P. F.; Korgel, B. A. *J. Am. Chem. Soc.* **2008**, *130*, 16770.
(13) Riha, S. C.; Parkinson, B. A.; Prieto, A. L. *J. Am. Chem. Soc.* **2009**, *131*, 12054.
(14) Chesman, A. S. R.; Duffy, N. W.; Peacock, S.; Waddington, L.; Webster, N. A. S.; Jasieniak, J. J. *RSC Adv.* **2013**, *3*, 1017.
(15) Guo, Q.; Ford, G.; Yang, W.-C.; Walker, B.; Stach, E.; Hillhouse, H.; Agrawal, R. *J. Am. Chem. Soc.* **2010**, *132*, 17384.
(16) Chesman, A. S. R.; van Embden, J.; Duffy, N. W.; Webster, N. A. S.; Jasieniak, J. J. *Cryst. Growth Des.* **2013**, *13*, 1712.
(17) Norako, M. E.; Greaney, M. J.; Brutchey, R. L. *J. Am. Chem. Soc.* **2012**, *134*, 23.
(18) Shavel, A.; Arbiol, J.; Cabot, A. *J. Am. Chem. Soc.* **2010**, *132*, 4514.
(19) Wadia, C.; Wu, Y.; Gul, S.; Volkman, S. K.; Guo, J.; Alivisatos, A. P. *Chem. Mater.* **2009**, *21*, 2568.
(20) Puthussery, J.; Seefeld, S.; Berry, N.; Gibbs, M.; Law, M. *J. Am. Chem. Soc.* **2011**, *133*, 716.
(21) Yan, C.; Huang, C.; Yang, J.; Liu, F.; Liu, J.; Lai, Y.; Li, J.; Liu, Y. *Chem. Commun.* **2012**, *48*, 2603.
(22) Hickey, S. G.; Waurisch, C.; Rellinghaus, B.; Eychmuller, A. *J. Am. Chem. Soc.* **2008**, *130*, 14978.
(23) Soriano, R.; Arachchige, I.; Malliakas, C.; Wu, J.; Kanatzidis, M. *J. Am. Chem. Soc.* **2013**, *135*, 768.
(24) Karkamkar, A.; Kanatzidis, M. *J. Am. Chem. Soc.* **2006**, *128*, 6002.
(25) Mehta, R.; Karthik, C.; Jiang, W.; Singh, B.; Shi, Y.; Siegel, R.; Borca-Tasciuc, T.; Ramanath, G. *Nano Lett.* **2010**, *10*, 4417.
(26) Liu, W.; Chang, A.; Schaller, R.; Talapin, D. *J. Am. Chem. Soc.* **2012**, *134*, 20258.
(27) Im, S.; Lim, C.-S.; Chang, J.; Lee, Y.; Maiti, N.; Kim, H.-J.; Nazeeruddin, M.; Gratzel, M.; Seok, S. *Nano Lett.* **2011**, *11*, 4789.
(28) Moon, S.-J.; Itzhaik, Y.; Yum, J.-H.; Zakeeruddin, S. M.; Hodes, G.; Gratzel, M. *J. Phys. Chem. Lett.* **2010**, *1*, 1524.
(29) Maiello, P.; Zoppi, G.; Forbes, I.; Miles, R. W.; Pearsall, N. The 7th Photovoltaic Science Applications and Technology conference, 2011.
(30) Jeanloz, R.; Johnson, M. L. *Phys. Chem. Miner.* **1984**, *11*, 52.
(31) Skoug, E. J.; Cain, J. D.; Morelli, D. T. a. K., M.; Majsztrik, P.; Lara-Curzio, E. *Appl. Phys. Lett.* **2011**, *110*, 023501.
(32) Amirkhanov, K. I.; Gadzhiev, G. G.; Magomedov, Y. B. *High Temp.* **1978**, *16*, 1050.
(33) Jin-Hui, D.; Zhen-Rui, Y.; Jia-You, Z. *Electron. Compon. Mater.* **2005**, *24*, 24.
(34) Rabhi, A.; Kanzari, M.; Rezig, B. *Mater. Lett.* **2008**, *62*, 3576.
(35) Rabhi, A.; Kanzari, M. *Chalcogenide Lett.* **2011**, *8*, 255.
(36) van Embden, J.; Tachibana, Y. *J. Mater. Chem.* **2012**, *22*, 11466.
(37) Yan, C.; Su, Z.; Gu, E.; Cao, T.; Jia, Y.; Liu, J.; Liu, F.; Lai, Y.; Li, J.; Liu, Y. *RSC Adv.* **2012**, *2*, 10481.
(38) Mott, D.; Yin, J.; Engelhard, M.; Loukrakpam, R.; Chang, P.; Miller, G.; Bae, I.-T.; Das, N. C.; Wang, C.; Luo, J.; Zhong, C.-J. *Chem. Mater.* **2010**, *22*, 261.
(39) Wang, Y.; Hu, Y.; Zhang, Q.; Ge, J.; Lu, Z.; Hou, Y.; Yin, Y. *Inorg. Chem.* **2010**, *49*, 6601.
(40) Wuensch, B. J. *Science* **1963**, *141*, 804.
(41) Jiasong, Z.; Weidong, X.; Huaidong, J.; Wen, C.; Lijun, L.; Xinyu, Y.; Xiaojuan, L.; Haitao, L. *Mater. Lett.* **2010**, *64*, 1499.
(42) Wedemeyer, H.; Michels, J.; Chmielowski, R.; Bourdais, S.; Muto, T.; Sugiura, M.; Dennler, G.; Bachmann, J. *Energy Environ. Sci.* **2013**, *6*, 67.
(43) Zivkovic, Z.; Strbac, N.; Zivkovic, D.; Grujicic, D.; Boyanov, B. *Thermochim. Acta* **2002**, *383*, 137.
(44) Wells, R.; Pitt, C. G.; McPhail, T.; Purdy, A. P.; Schafieezad, S.; Hallock, R. B. *Chem. Mater.* **1989**, *1*, 4.
(45) Wells, R. L.; Gladfelter, W. L. *J. Cluster Sci.* **1997**, *8*, 217.
(46) Pradhan, N.; Reifsnyder, D.; Xie, R.; Aldana, J.; Peng, X. *J. Am. Chem. Soc.* **2007**, *129*, 9500.
(47) van Embden, J.; Mulvaney, P. *Langmuir* **2005**, *21*, 10226.
(48) Bullen, C. R.; Mulvaney, P. *Nano Lett.* **2004**, *4*, 2303.
(49) Ghezelbash, A.; Korgel, B. *Langmuir* **2005**, *21*, 9451.
(50) Zhuang, Z.; Peng, Q.; Zhang, B.; Li, Y. *J. Am. Chem. Soc.* **2008**, *130*, 10482.
(51) Kuzuya, T.; Itoh, K.; Sumiyama, K. *J. Colloid Interface Sci.* **2008**, *319*, 565.
(52) Lu, Q.; Gao, F.; Zhao, D. *Nano Lett.* **2002**, *2*, 725.
(53) Connor, S.; Hsu, C.; Weil, B.; Aloni, S.; Cui, Y. *J. Am. Chem. Soc.* **2009**, *131*, 4962.
(54) Coughlan, C.; Singh, A.; Ryan, K. M. *Chem. Mater.* **2013**, *25*, 653.
(55) Steinhagen, C.; Panthani, M.; Akhavan, V.; Goodfellow, B.; Koo, B.; Korgel, B. *J. Am. Chem. Soc.* **2009**, *131*, 12554.
(56) Shavel, A.; Cadavid, D.; Ibanez, M.; Carrete, A.; Cabot, A. *J. Am. Chem. Soc.* **2012**, *134*, 1438.
(57) Kar, M.; Agrawal, R.; Hillhouse, H. *J. Am. Chem. Soc.* **2011**, *133*, 17239.
(58) Jeanolz, R.; Johnson, M. L. *Phys. Chem. Miner.* **1984**, *11*, 52.
(59) Liu, W. C.; Guo, B. L.; Wu, X. S.; Zhang, F. M.; Mak, C. L.; Wong, K. H. *J. Mater. Chem. A* **2013**, *1*, 3182.
(60) Khare, A.; Wills, A.; Ammerman, L.; Norris, D.; Aydil, E. *Chem. Commun.* **2011**, *47*, 11721.
(61) Luther, J.; Jain, P.; Ewers, T.; Alivisatos, A. *Nat. Mater.* **2011**, *10*, 361.
(62) Katsuhiro, N.; Takahisa, O.; Shinya, O.-Y.-M. *J. Phys. Chem. C* **2009**, *113*, 3455.
(63) Dannhauser, T.; Neil, M. O.; Johansson, K.; Whitten, D.; McLendon, G. *J. Phys. Chem.* **1986**, *90*, 6074.
(64) Zhao, Y.; Pan, H.; Lou, Y.; Qiu, X.; Zhu, J.; Burda, C. *J. Am. Chem. Soc.* **2009**, *131*, 4253.
(65) Pattrick, R. A. D.; Laan, G.; Vaughan, D. J.; Henderson, C. M. B. *Phys. Chem. Miner.* **1993**, *20*, 395.

(66) Buckley, A. N.; Skinner, W. M.; Harmer, S. L.; Pring, A.; Lamb, R. N.; Fan, L.-J.; Yang, Y.-W. *Can. J. Chem.* **2007**, *85*, 767.
(67) An, C.; Jin, Y.; Tang, K.; Qian, Y. *J. Mater. Chem.* **2003**, *13*, 301.
(68) Biesinger, M. C.; Lau, L. W. M.; Gerson, A. R.; Smart, R. S. C. *Appl. Surf. Sci.* **2010**, *257*, 887.
(69) Krylova, V.; Andrulevicius, M. *Int. J. Photoenergy* **2009**, *2009*, 304308.
(70) Nogueira, A. F.; Longo, C.; Paoli, M. A. D. *Coord. Chem. Rev.* **2004**, *248*, 1455.
(71) Li, B.; Liduo, W.; Kang, B.; Wang, P.; Qiu, Y. *Sol. Energy Mater. Sol. Cells* **2006**, *90*, 549.
(72) Mingkui, W.; Carole, G.; Shaik, M. Z.; Michael, G. *Energy Environ. Sci.* **2012**, *5*, 9394.
(73) Riha, S.; Fredrick, S.; Sambur, J.; Liu, Y.; Prieto, A.; Parkinson, B. *ACS Appl. Mater. Interfaces* **2011**, *3*, 58.
(74) Webber, D.; Brutchey, R. *J. Am. Chem. Soc.* **2012**, *134*, 1085.
(75) Korala, L.; Wang, Z.; Liu, Y.; Maldonado, S.; Brock, S. *ACS Nano* **2013**, *7*, 1215.
(76) Steinhagen, C.; Harvey, T. B.; Stolle, C. J.; Harris, J.; Korgel, B. A. *J. Phys. Chem. Lett.* **2012**, *3*, 2352−2356.
(77) Todorov, T.; Reuter, K.; Mitzi, D. *Adv. Mater.* **2010**, *22*, E156.
(78) Mitzi, D. B.; Yuan, M.; Liu, W.; Kellock, A. J.; Jay Chey, S.; Deline, V.; Schrott, A. G. *Adv. Mater.* **2008**, *20*, 3657.
(79) Talapin, D.; Murray, C. *Science* **2005**, *310*, 86.
(80) Drndic, M.; Jarosz, M. V.; Morgan, N. Y.; Kastner, M. A.; Bawendi, M. G. *J. Appl. Phys.* **2002**, *92*, 7498.